

5B.2 TRENDS IN THE NORTHERN MIDLATITUDE ROSSBY WAVE IN A FUTURE CLIMATE

Heather S. Sussman*, Ajay Raghavendra, Paul E. Roundy, and Aiguo Dai
University at Albany, State University of New York, Albany, NY, USA

ABSTRACT

In a warming climate, atmospheric wave activity and subsequent weather patterns may change. Here, changes in planetary and shorter-scale Rossby waves are analyzed using the wavenumber-frequency power spectrum, a tool commonly applied to analyze atmospheric equatorial waves. We analyze daily data of 500 hPa geopotential height over 40°N–60°N from historical and future simulations by 20 models in the Coupled Model Intercomparison Project Phase 5 (CMIP5) under the RCP8.5 scenario. Results show that longwaves (wavenumbers 1–6) of 1–2 weeks increase in power from 1950–2099 during winter and spring, whereas shortwaves (wavenumber 8–20) of 2–7 days decrease in power for all seasons. This implies that large-scale (10^4 km) weather systems in winter and spring may intensify, while short-scale (10^2 – 10^3 km) features influencing day-to-day weather may weaken. We discuss potential mechanisms for these changes, including enhanced surface Arctic warming and midlatitude-tropical interactions.

Key words: Atmospheric Rossby waves, CMIP5, midlatitude climate change, wavenumber–frequency power spectrum.

1. Introduction

Atmospheric Rossby waves contain a variety of wave characteristics that influence the Northern Hemisphere jet stream and weather systems. These wave characteristics include longwaves (i.e., planetary-scale waves of 10^4 km), which influence weather variability mainly on 1–2 week time scales, and shortwaves, which are small-scale wave features (10^2 – 10^3 km) embedded within the longwaves that have a large influence on day-to-day weather variability. These wave motions interact with each other to form the northern midlatitude circulation (e.g., jet stream location and strength). Several recent studies suggest that in a future, warmer climate, the position and strength of the jet stream may change. This includes a poleward migration of the Northern Hemisphere jet stream (Yin, 2005; Barnes and Polvani, 2013) and associated northward shifts of the storm track regions (Bengtsson et al., 2006), and the possibility for intensified cyclones in the northern midlatitudes (Zappa et al., 2013; Feser et al., 2015). Studies have also indicated that the wavelength of baroclinic eddies (i.e., shortwaves) may increase in response to increasing greenhouse gases (GHGs), accompanied by a poleward shift in the midlatitude jet stream (Kidston et al., 2010, 2011). These results imply that increasing GHGs may change midlatitude wave activity, which in turn could alter the frequency, intensity, and duration of weather events in the region.

However, uncertainty remains regarding changes in the characteristics of midlatitude waves, which ultimately control the frequency, intensity, and duration of weather events. For example, Screen and Simmonds (2013) used two methods to quantify

amplitude changes in Rossby waves (wavenumbers 1–10) from 1979–2011 over different northern midlatitude longitude sectors, and results showed that trends in amplitude may be method dependent. This method dependency was also illustrated in Barnes (2013), where two methods were used to quantify amplitude changes from 1980–2011 over the North American/North Atlantic sector of the midlatitudes for Rossby waves (wavenumbers 1–6), and similarly results differed. Using one metric from Barnes (2013), Barnes and Polvani (2015) and hereafter BP15 analyzed changes in Rossby wave (wavenumbers 1–6) amplitude in a future climate, but results showed weak model agreement on the sign of the change. Furthermore, BP15 found weak model agreement on the sign of the change in wave speed in a future climate. However, blocking frequency (i.e., duration) was found to robustly decrease in all seasons in a future climate in BP15. Overall, more work is needed on understanding changes in northern midlatitude wave activity, particularly for longwaves and shortwaves separately, in a future climate since weather patterns affect transportation, agriculture, and commerce (Francis, 2017).

Here, we utilize the wavenumber-frequency power spectrum that is commonly found in tropical atmospheric equatorial wave analysis (Wheeler and Kiladis, 1999 and hereafter WK99) to quantify changes in the distribution of spectral power of midlatitude atmospheric waves from 1950–2099, with a focus on longwaves and shortwaves. These changes in the time-mean power reflect changes in wave amplitude, frequency of occurrence, and duration. Recently, Raghavendra et al., (2019) showed that the wavenumber-frequency power spectrum can be used to quantify changes in tropical atmospheric wave power during the satellite era (i.e., since 1979), and found that high-frequency waves (e.g., Kelvin waves, mixed Rossby gravity waves, and tropical depression-type disturbances) have experienced an increase in

* *Corresponding author address:* Heather S. Sussman, Dept. of Atmospheric and Environmental Sciences, University at Albany, 1400 Washington Ave., Albany, NY–12222; e-mail: hsussman@albany.edu

power since 1979. Here we apply a similar framework as Raghavendra et al., (2019), but for northern midlatitude atmospheric zonal waves projected by multiple climate models for the 21st century. We first compare the wavenumber-frequency power spectra for the northern midlatitudes from the historical simulations by 20 models in the Coupled Model Intercomparison Project Phase 5 (CMIP5; Taylor et al., 2012) with those from reanalyses, and then examine their future change under the RCP8.5 high emissions scenario, with a focus on eastward propagating longwaves (wavenumbers 1–6) and shortwaves (wavenumbers 8–20). We conclude by discussing some potential mechanisms for these changes, including a possible role of Arctic amplification (AA), which refers to the enhanced surface warming over the Arctic when compared to the rest of the world that is likely to be caused by sea-ice loss (Screen and Simmonds, 2010; Dai et al., 2019), which may impact northern midlatitude circulation through the reduction in the Arctic–midlatitude meridional temperature gradient (Francis and Vavrus, 2012).

2. Data and Methods

a) Study Region and Data

We focus on wave activity over the entire Northern Hemisphere midlatitudes from 40°–60°N. We tested other slightly different definitions of the northern midlatitudes and found similar results. Daily data for 500 hPa geopotential height (Z500) were utilized in the spectral analysis, as planetary- and synoptic-scale waves are best diagnosed using this field (BP15). We obtained these data from 20 CMIP5 models (Table S1; Taylor et al. 2012) for the historical period (1950–2005) and future projections (2006–2099) under the RCP8.5 high emissions scenario, with one ensemble member for each model. For model evaluation, we analyzed Z500 daily data from 1979–2005 from both the European Centre for Medium-Range Weather Forecasts' ERA-Interim reanalysis (Dee et al., 2011) and the National Centers for Environmental Prediction/National Center for Atmospheric Research Reanalysis-2 (NCEP/NCAR-2; Kanamitsu et al., 2002). The wavenumber-frequency power spectra looked remarkably similar for these reanalysis products; thus, only the ERA-Interim results are shown here. The daily Z500 fields from the reanalyses and the CMIP5 models were linearly interpolated onto a 2.0° × 2.0° grid before the spectral analysis to minimize the impact of different data resolutions.

b) Wavenumber-frequency power spectrum

The seasonal cycle was removed before the spectral analysis (WK99) by the following Fourier regression model:

$$C = (X^T \times X)^{-1} \times X^T \times Y, \quad (1)$$

where Y is the time series of Z500 data over the study region and time period of interest of the respective dataset (i.e., reanalysis or CMIP5 model) and X is the

predictor matrix that consists of a column of ones that is the length of the number of the days within the dataset and remaining columns consist of sine and cosine pairs that represent the first five harmonics of the seasonal cycle (Roundy, 2018). The seasonal cycle (i.e., $X \times C$) was calculated and then subtracted from Y to obtain daily Z500 anomalies (i.e., Y_{anom}).

Y_{anom} was then segmented in time using 62-day time windows that overlap by one-half. The time windows were detrended and tapered to zero using a Hann window (i.e., a cosine bell) to prevent spectral leakage (WK99). A 62-day time window was chosen such that the time scales of interest in this study (i.e., variability within the 2–14 day range) could be properly resolved. A 2-dimensional fast Fourier transform (FFT) was then applied to each data segment to obtain $\text{FFT}(Y_{\text{anom}})$ at each latitude. This transforms Y_{anom} from a 3-dimensional variable of (time, latitude, longitude) to a 4-dimensional variable of (latitude, frequency, wavenumber, segment number). Power was then computed by:

Power = $\log_e [\text{FFT}(Y_{\text{anom}}) \times \text{conj}(\text{FFT}(Y_{\text{anom}}))]$, (2)
where $\text{conj}[\text{FFT}(Y_{\text{anom}})]$ is the complex conjugate of $\text{FFT}(Y_{\text{anom}})$. Here, \log_e is included in the **Power** computation for visualization as the values of **Power** are on the order of 10^6 – 10^9 . Our conclusions are not sensitive to the utilization of $\log_e(\text{Power})$.

Since there is seasonality associated with the northern midlatitude storm track regions (Chang et al., 2002), it is necessary for changes in northern midlatitude spectral power to be analyzed by season. To obtain seasonal power spectra, we constructed a Hermite Polynomial of the form $P(x) = 1 - 3x^2 + 2x^3$, where $x \in [0, 1]$ with a 20-day smoother, such that the 10 days before a new season and 10 days after are transitioned smoothly in order to avoid Gibbs Ringing Phenomenon when sectioning the data by season (Raghavendra and Guinn, 2016). Furthermore, x is zero if the day is not in the respective season, is one if contained within the respective season, and is a fraction between zero and one if contained within ± 10 days before a change in season. We multiplied Y_{anom} by the Hermite Polynomial for each season to derive the seasonal data series, with seasons defined as December-January-February (DJF), March-April-May (MAM), June-July-August (JJA), and September-October-November (SON). Power was then computed following Eq. (2) using the seasonal data series. The seasonal power for each year was obtained by averaging over all the time windows within each season (approximately 2–3 windows) and over all latitudes within 40°–60°N.

The wave power spectra show different change patterns for the longwaves, defined as waves with wavenumbers 1–6 and period of 7–14 days (outlined by the black box in Figs. 1–2), and the shortwaves, defined as waves with wavenumbers 8–20 and period of 2–7 days (outlined by the red box in Figs. 1–2). Thus, we will focus on changes in these waves. We

recognize that our chosen longwave and shortwave regions do not represent the respective waves of all time scales. Our goal is to document changes in power for the longwaves that influence the eastward propagation of weather variability on a 1–2 week time scale and for shortwaves that influence the eastward propagation of day-to-day weather only. We first computed the relative percentage change from 1980–1999 to 2080–2099 in the mean power for the entire spectrum. We then calculated the spatial patterns of the trends during 1950–2099 in the longwave and shortwave power. This was achieved by taking the FFT^{-1} (inverse of FFT) of the transformed Z500 anomaly data including only the Fourier coefficients that are within the wave region of interest in the wavenumber-frequency domain (e.g., WK99; Roundy and Frank, 2004; Raghavendra et al., 2019). We then squared the filtered anomalies to compute variance and regressed them against time to estimate trends. Lastly, we computed the seasonal time series from 1950–2099 of the mean wavenumber-frequency power spectra (calculated separately for each season) for longwaves and shortwaves to examine how the power within those two regions evolves from 1950–2099. For each analysis, statistical significance was calculated using the two-tailed Student's t-test, with a p-value ≤ 0.05 considered statistically significant.

3. Results

a) Model evaluation

The 1979–2005 mean wavenumber-frequency power spectra for ERA-Interim and the 20 CMIP5 model mean for DJF and JJA are shown in Figure 1. The spectra produced by ERA-Interim (Figs. 1a–1b) and the CMIP5 ensemble mean (Figs. 1c–1d) are remarkably similar for both seasons. This is also true of the MAM and SON spectra (not shown). This suggests that the models can simulate the current power spectrum for the planetary and shorter waves, which provides some confidence for us to examine their simulated future changes. Figure 1 shows that the mean wave power is higher in DJF than in JJA in both ERA-Interim and CMIP5 models, which is consistent with the stronger wave and weather variability seen in northern midlatitude winter. The values of power for MAM and SON are similar to each other, and slightly less than that of DJF. Furthermore, the longwave band has higher power than that of the shortwave band in both seasons, which suggests that the amplitude, frequency of occurrence, and/or duration are higher for the longwaves than for the shortwaves.

b) Power changes

The relative percentage change from 1980–1999 to 2080–2099 in seasonal wave power for the entire spectrum is shown in Figure 2. For wavenumbers greater than 8, a decrease in power is shown over all frequencies for all seasons, especially in JJA and SON. For DJF, MAM, and SON (Figs. 2a, 2b, and 2d), an

increase in power is shown over a narrow band of the spectrum in the eastward direction around wavenumbers 1–6. This is not the case for JJA (Fig. 2c), where no increase in power is shown in this region. These results suggest a shift in power from higher wavenumbers to lower wavenumbers for DJF, MAM, and SON, which is consistent with the results of Kidston et al. (2010), who suggested an increase in the mean wavelength in response to high GHG emissions.

Figure 3 shows the spatial distribution of the trend in variance during 1950–2099 for the longwaves and shortwaves (i.e., regions outlined by the black and red boxes in Figs. 1–2, respectively) for each season. For the longwaves (Figs. 3a–3d), significant positive trends are seen over the North Atlantic and Europe and parts of western Asia in DJF and MAM, as well as parts of the western North Pacific in MAM, while increases are seen mostly over the northern North Pacific and northern North America in SON (Fig. 3d). For JJA (Fig. 3c), most of the trends are statistically insignificant, with some decreases over the northeastern North Pacific and some increases over the North Atlantic and central North America, which thus results in mostly insignificant changes for this wave region (i.e., the black box in Fig. 2c). For the shortwaves (Figs. 3e–3h), significant declines in variance are seen over most of the northern midlatitudes, especially for SON, JJA, and MAM, consistent with the wave power changes shown by the red box in Fig. 2.

The temporal evolution of mean \log_e spectral power is shown for the longwaves in Fig. 4a and shortwaves in Fig. 4b. The upward trends in the time series for the longwaves are significant only for DJF and MAM, which is consistent with the variance trend maps shown in Figs. 3a–d. This translates to a wave activity and variability increase for the longwaves due to either an increase in their amplitude (i.e., increased waviness; Martin et al., 2019) and/or frequency of occurrence. The downward trends in the time series for the shortwaves are significant for all seasons, especially for JJA and SON, again confirming the changes shown in Figs. 2 and 3e–h, and translating to a wave activity and variability decrease for the shortwaves due to either a decrease in their amplitude and/or occurrence frequency. Overall, a redistribution of power from the shortwaves to the longwaves is observed for all seasons as the shortwaves decline in power while the longwaves increase in power or change little. The respective changes in power are not due to changes in duration as the redistribution of power we observe only shows a spatial scale redistribution of power rather than a temporal scale change, i.e., power at low wavenumbers increases and power at high wavenumbers increases (Fig. 3).

c) Potential physical mechanisms

The wave power changes discussed above are a part of the northern midlatitude response to GHG-induced global warming under the RCP8.5 high

emissions scenario. But there are several possible mechanisms whereby climate change might yield this outcome. Besides the local warming response, changes at remote latitudes may influence these changes in the wave spectrum in this study region. To investigate any potential remote factors, we computed the 2080–2099 minus 1980–1999 differences in zonal-mean air temperature (T) and meridional temperature gradient ($\frac{dT}{dy}$) over the Northern Hemisphere for each season using monthly air temperature data from the 20 CMIP5 models listed in Table S1 on a $2.0^\circ \times 2.0^\circ$ grid (Fig. 5).

From Figure 5, we observe the AA signal, and find it to be strongest in DJF, MAM, and SON, and of small magnitude in JJA. This is in agreement with Dai et al., (2019), who found that strong AA mainly occurs from October to April. Strong AA should reduce the meridional temperature gradient, as the Arctic warms faster than the lower latitudes. This could lead to a reduction in zonal wind through the thermal wind relationship, and a weakened zonal wind favors larger amplitudes of zonal waves and atmospheric blocking (Luo et al., 2014, 2017, 2018). Because of this, it has been proposed that AA and the associated reduction in the meridional temperature gradient between the Arctic and the midlatitudes may cause Rossby waves to elongate meridionally, while slowing down in their eastward propagation (Francis and Vavrus, 2012). This mechanism may increase the persistence of weather conditions (e.g., Dole et al., 2011). For DJF, MAM, and SON (Figs. 5a, 5b, and 5d), a clear decrease in $\frac{dT}{dy}$ in the lower troposphere from the Arctic toward the midlatitudes is observed. This could cause some changes in zonal wind over these regions, which may in turn affect wave activities in the midlatitudes. However, it is unclear how exactly the $\frac{dT}{dy}$ change may alter wave activity at the preferred scales discussed. Furthermore, the $\frac{dT}{dy}$ changes in JJA is small, yet the decrease in JJA shortwave activity is robust (Figs. 2c, 3g, and 4b). This suggests other mechanisms for our results, especially in JJA.

Another potential remote mechanism may come from the low latitudes. For example, the poleward expansion of the Hadley cell circulation (Fu, 2015; Byrne and Schneider, 2016a, 2016b) may decrease the meridional temperature gradient between the subtropics and the midlatitudes due to changes in ocean heat transport (Rencurrel and Rose, 2018), albeit this temperature gradient decrease is weak when compared to the Arctic–midlatitude temperature gradient decrease (Fig. 5). Additionally, changes in the distribution of rainfall events in the tropics can also influence wave propagation across the middle latitudes, because tropical convection is one source of midlatitude wave activity (Baggett et al., 2016). Also, heating near the Northern midlatitude region associated with desert amplification (Zhou, 2016) may

also reduce the subtropical-midlatitude meridional temperature gradient. Further investigations are needed on how the low-latitude changes may influence northern midlatitude longwaves and shortwaves (e.g., Peings et al., 2017).

4. Conclusions

We have examined the model projected changes from 1950–2099 in the spectral power of zonal waves over the northern midlatitudes (40° – 60° N) in daily Z500 from 20 CMIP5 models using the wavenumber-frequency power spectrum to understand how wave activity in this region may behave in a future, warmer climate. The CMIP5 models reproduce the mean wave power spectra seen in ERA-Interim and other reanalyses well. Under the RCP8.5 high emissions scenario, the models project a significant decrease during the 21st century in wave power for shortwaves (i.e., wavenumbers 8–20 and period of 2–7 days) for all seasons, especially for JJA and SON, but significant increases in wave power for longwaves (i.e., wavenumbers 1–6 and period of 7–14 days) for DJF and MAM. The weakening of the shortwaves is seen over most of the longitudes, while the strengthening of the longwaves is concentrated from the North Atlantic to Europe in DJF and MAM.

Our results suggest a shift of zonal wave power from high wavenumbers (>7) towards eastward propagating Rossby waves with wavenumbers of 1–6. Since wave power reflects time-averaged wave amplitude, these results suggest that the time-averaged amplitude of the longwaves in DJF and MAM would increase in the 21st century, while the time-averaged amplitude for the shortwaves in all seasons would decrease. This implies that the longwaves would become either stronger when they occur and/or occur more frequently, while the shortwaves would become either weaker and/or occur less frequently. As a result, large-scale planetary weather patterns (mainly on timescales of 7–14 days) in DJF and MAM may intensify in the 21st century, while smaller-scale cyclones and anticyclones (including timescales of 2–7 days) may weaken (Fig. 2).

Although the wave power changes are likely part of the midlatitude response to GHG-induced global warming, GHG-induced changes in the Arctic and lower latitudes may also impact the midlatitude wave spectrum because these regions can be sources of wave activity. For example, AA reduces the Arctic–midlatitude temperature gradient and thus may influence midlatitude circulation and zonal wave activities. Other influences may come from the poleward expansion of the Hadley cell under global warming or changes in the distribution and variability of tropical rainfall. Further investigations of the physical mechanisms underlying the midlatitude zonal wave changes are needed.

Acknowledgements.

We thank the CMIP5 modeling groups, the Program for Climate Model Diagnosis and Intercomparison and the WCRP's Working Group on Coupled Modelling for their efforts in making the CMIP5 multi-model dataset listed in Table S1 available through the Earth System Grid Federation (<https://esgf-node.llnl.gov/projects/esgf-llnl/>). Heather S. Sussman and Aiguo Dai acknowledge the funding support from the National Science Foundation (AGS-1353740 and OISE-1743738), the U.S. Department of Energy's Office of Science (DE-SC0012602), and the U.S. National Oceanic and Atmospheric Administration (NA15OAR4310086). Ajay Raghavendra acknowledges funding support from NSF AGS-1535426, and Paul E. Roundy acknowledges funding support from NSF AGS-1358214 and AGS-1128779. The authors also thank Dr. Elizabeth A. Barnes for insightful discussions that helped to improve the quality of this work.

References

Arora, V. K., J. F. Scinocca, G. J. Boer, J. R. Christian, K. L., Denman, G. M. Flato, Kharin, V. V., Lee, W. G., and Merryfield, W. J., 2011: Carbon emission limits required to satisfy future representative concentration pathways of greenhouse gases. *Geophys. Res. Lett.*, **38**, L05805.

Baggett, C., and S. Lee, 2015: Arctic warming induced by tropically forced tapping of available potential energy and the role of the planetary-scale waves. *J. Atmos. Sci.*, **72**, 1562–1568.

Barnes, E. A., 2013: Revisiting the evidence linking Arctic amplification to extreme weather in midlatitudes. *Geophys. Res. Lett.*, **40**, 4734–4739.

Barnes, E. A., and L. Polvani, 2013: Response of the midlatitude jets, and of their variability, to increased greenhouse gases in the CMIP5 models. *J. Climate*, **26**, 7117–7135.

Barnes, E. A., and L. M. Polvani, 2015: CMIP5 projections of Arctic amplification, of the North American/North Atlantic circulation, and of their relationship. *J. Climate*, **28**, 5254–5271.

Bengtsson, L., K. I. Hodges, and E. Roeckner, 2006: Storm tracks and climate change. *J. Climate*, **19**, 3518–3543.

Bentsen, M., and Coauthors, 2013: The Norwegian Earth System Model, NorESM1-M—Part 1: Description and basic evaluation of the physical climate. *Geosci. Model Dev.*, **6**, 687–720.

Byrne, M. P., and T. Schneider, 2016a: Energetic constraints on the width of the intertropical convergence zone. *J. Climate*, **29**, 4709–4721.

Byrne, M. P., and T. Schneider, 2016b: Narrowing of the ITCZ in a warming climate: Physical mechanisms. *Geophys. Res. Lett.*, **43**, 11350–11357.

Chang, E. K. M., S. Lee, and K. L. Swanson, 2002: Storm track dynamics. *J. Climate*, **15**, 2163–2183.

Collier, M., and P. Uhe, 2012: CMIP5 datasets from the ACCESS1.0 and ACCESS1.3 coupled climate models. Centre for Australian Weather and Climate Research Tech. Rep. 059, 25 pp. [Available at http://www.cawcr.gov.au/technical-reports/CTR_059.pdf].

Dai, A., D. Luo, M. Song, and J. Liu, 2019: Arctic amplification is caused by sea-ice loss under increasing CO₂. *Nat. Commun.*, **10**, 1–13.

Dee, D., and Coauthors, 2011: The ERA-Interim reanalysis: Configuration and performance of the data assimilation system. *Quart. J. Roy. Meteor. Soc.*, **137**, 553–597.

Dole, R., and Coauthors, 2011: Was there a basis for anticipating the 2010 Russian heat wave? *Geophys. Res. Lett.*, **38**, L06702.

Dufresne, J.-L., and Coauthors, 2013: Climate change projections using the IPSL-CM5 Earth System Model: From CMIP3 to CMIP5. *Climate Dyn.*, **40**, 2123–2165.

Donner, L. J., and Coauthors, 2011: The dynamical core, physical parameterizations, and basic simulation characteristics of the atmospheric component AM3 of the GFDL global coupled model CM3. *J. Climate*, **24**, 3484–3519.

Giorgetta, M. A., and Coauthors, 2013: Climate and carbon cycle changes from 1850 to 2100 in MPI-ESM simulations for the Coupled Model Intercomparison Project phase 5. *J. Adv. Model. Earth Syst.*, **5**, 572–597.

Griffies, S. M., and Coauthors, 2011: GFDL's CM3 coupled climate model: Characteristics of the ocean and sea ice simulations. *J. Climate*, **24**, 3520–3544.

Feser, F., M. Barcikowska, O. Krueger, F. Schenk, R. Weiss, and L. Xia, 2015: Storminess over the North Atlantic and northwestern Europe—A review. *Quart. J. Roy. Meteor. Soc.*, **141**, 350–382.

Fogli, F. G., E. Manzini, M. Vichi, A. Alessandri, L. Patara, S. Gualdi, E. Scoccimarro, S. Masina, and A. Navarra, 2009: INGV-CMCC carbon (ICC): A carbon cycle Earth system model, CMCC Res. Pap. 61, Euro-Mediterr. Cent. for Clim. Change, Lecce, Italy. [Available at <http://ssrn.com/abstract=1517282>].

Francis, J. A., 2017: Why are Arctic linkages to extreme weather still up in the air? *Bull. Amer. Meteor. Soc.*, **98**, 2551–2557.

Francis, J. A., and S. J. Vavrus, 2012: Evidence linking Arctic amplification to extreme weather in mid-latitudes. *Geophys. Res. Lett.*, **39**, L06801.

Fu, R., 2015: Global warming-accelerated drying in the tropics. *Proc. Natl. Acad. Sci. USA*, **112**, 3593–3594.

Jones, C., and Coauthors, 2011: The HadGEM2-ES implementation of CMIP5 centennial simulations. *Geosci. Model Dev.*, **4**, 543–570.

Kanamitsu, M., W. Ebisuzaki, J. Woollen, S.-H. Yang, J. J. Hnilo, M. Fiorino, and G. L. Potter, 2002: NCEP–

- DOE AMIP-II Reanalysis (R-2). *Bull. Amer. Meteor. Soc.*, **83**, 1631–1643.
- Kidston, J., S. Dean, J. Renwick, and G. K. Vallis, 2010: A robust increase in the eddy length scale in the simulation of future climates. *Geophys. Res. Lett.*, **37**, L03806.
- Kidston, J., G. K. Vallis, S. M. Dean, and J. Renwick, 2011: Can the increase in the eddy length scale under global warming cause the poleward shift of the jet streams? *J. Climate*, **24**, 3764–3780.
- Luo, D., J. Cha, L. Zhong, and A. Dai, 2014: A nonlinear multiscale interaction model for atmospheric blocking: The eddy-blocking matching mechanism. *Quart. J. Roy. Meteor. Soc.*, **140**, 1785–1808.
- Luo, D., Y. Yao, A. Dai, I. Simmonds, and L. Zhong, 2017: Increased quasi stationarity and persistence of winter Ural blocking and Eurasian extreme cold events in response to Arctic warming. Part II: A theoretical explanation. *J. Climate*, **30**, 3569–3587.
- Luo, D., X. Chen, A. Dai, and I. Simmonds, 2018: Changes in atmospheric blocking circulations linked with winter Arctic warming: A new perspective. *J. Climate*, **31**, 7661–7678.
- Martin, J. E., 2019: Evidence for increased waviness of the Northern Hemisphere wintertime polar and subtropical jets. *32nd Conf. on Climate Variability and Change*, Phoenix, AZ, Amer. Meteor. Soc., 5B.3, <https://ams.confex.com/ams/2019Annual/meetingapp.cgi/Paper/352837>.
- Peings, Y., J. Cattiaux, S. J. Vavrus, and G. Magnusdottir, 2017: Late twenty-first-century changes in the midlatitude atmospheric circulation in the CESM large ensemble. *J. Climate*, **30**, 5943–5960.
- Raghavendra, A., and T. A. Guinn, 2016: Breakdown of ITCZ-like PV patterns. *Beyond Undergrad. Res. Journal*, **1**, 1–11.
- Raghavendra, A., P. E. Roundy, and L. Zhou, 2019: Trends in tropical wave activity from 1980s–2016. *J. Climate*, (in press). doi: 10.1175/JCLI-D-18-0225.1
- Rencurrel, M. C., and B. E. J. Rose, 2018: Exploring the climatic response to wide variations in ocean heat transport on an aquaplanet. *J. Climate*, **31**, 6299–6318.
- Roundy, P. E., 2018: A wave-number frequency wavelet analysis of convectively coupled equatorial waves and the MJO over the Indian Ocean. *Quart. J. Roy. Meteor. Soc.*, **144**, 333–343.
- Roundy, P. E., and W. M. Frank, 2004: A climatology of waves in the equatorial region. *J. Atmos. Sci.*, **61**, 2105–2132.
- Screen, J. A., and I. Simmonds, 2010: The central role of diminishing sea ice in recent Arctic temperature amplification. *Nature*, **464**, 1334–1337.
- Taylor, K. E., R. J. Stouffer, and G. A. Meehl, 2012: An overview of CMIP5 and the experiment design. *Bull. Amer. Meteor. Soc.*, **93**, 485–498.
- Voltaire, A., and Coauthors, 2013: The CNRM-CM5.1 global climate model: Description and basic evaluation. *Climate Dyn.*, **40**, 2091–2121.
- Watanabe, M., and Coauthors, 2010: Improved climate simulation by MIROC5: Mean states, variability, and climate sensitivity. *J. Climate*, **23**, 6312–6335.
- Watanabe, S., and Coauthors, 2011: MIROC-ESM: Model description and basic results of CMIP5-20c3m experiments. *Geosci. Model Dev.*, **4**, 845–872.
- Wheeler, M., and G.N. Kiladis, 1999: Convectively Coupled Equatorial Waves: Analysis of Clouds and Temperature in the Wavenumber-Frequency Domain. *J. Atmos. Sci.*, **56**, 374–399.
- Yin, J. H., 2005: A consistent poleward shift of the storm tracks in simulations of 21st century climate. *Geophys. Res. Lett.*, **32**, L18701.
- Yukimoto, S., and Coauthors, 2011: Meteorological Research Institute Earth System Model Version 1 (MRI-ESM1)—Model Description—. *Technical Reports of the Meteorological Research Institute*, **64**, 83 pp. [Available at http://www.mri-jma.go.jp/Publish/Technical/DATA/VOL_64/index_en.html].
- Yukimoto, S., and Coauthors, 2012: A new global climate model of the Meteorological Research Institute: MRI-CGCM3—Model description and basic performance, *J. Meteor. Soc. Japan*, **90a**, 23–64.
- Zappa, G., L. C. Shaffrey, K. I. Hodges, P. G. Sansom, and D. B. Stephenson, 2013: A multimodel assessment of future projections of North Atlantic and European extratropical cyclones in the CMIP5 climate models. *J. Climate*, **26**, 5846–5862.
- Zhou, L., 2016: Desert amplification in a warming climate, *Scientific Reports*, **6**, 31065.

Tables and Figures

Table 1. Summary of the 20 CMIP5 models used in this study including the model name, model abbreviation, the institution that developed the model, the atmospheric resolution, and key model reference.

Ref. No.	Model Name (Abbreviation)	Institution	Atmospheric Resolution (lat × lon)	Key Reference
1	Australian Community Climate and Earth System Simulator, version 1 (ACCESS1-0)	Commonwealth Scientific and Industrial Research Organisation and Bureau of Meteorology Australia (CSIRO–BoM)	1.25° × 1.875°	Collier and Uhe (2012)
2	Australian Community Climate and Earth System Simulator, version 1-3 (ACCESS1-3)		1.25° × 1.875°	
3	Canadian Earth System Model, version 2 (CanESM2)	Canadian Centre for Climate Modelling and Analysis (CCCma)	2.8° × 2.8°	Arora et al. (2011)
4	Centro Euro-Mediterraneo per I Cambiamenti Climatici Carbon Earth System Model (CMCC-CESM)	Centro Euro-Mediterraneo per I Cambiamenti Climatici (CMCC)	3.4° × 3.75°	Fogli et al. (2009)
5	Centro Euro-Mediterraneo per I Cambiamenti Climatici Climate Model (CMCC-CM)		0.75° × 0.75°	
6	Centro Euro-Mediterraneo per I Cambiamenti Climatici Climate Model with a Resolved Stratosphere (CMCC-CMS)		3.7° × 3.75°	
7	Centre National de Recherches Meteorologiques Coupled Global Climate Model, version 5 (CNRM-CM5)	National Centre for Meteorological Research, France	1.4° × 1.4°	Voltaire et al. (2013)
8	Geophysical Fluid Dynamics Laboratory Climate Model, version 3 (GFDL-CM3)	National Oceanic and Atmospheric Administration (NOAA)	2.0° × 2.5°	Griffies et al. (2011)
9	Geophysical Fluid Dynamics Laboratory Earth System Model with Modular Ocean Model 4 (MOM4) ocean component (GFDL-ESM2M)	Geophysical Fluid Dynamics Laboratory	2.0° × 2.5°	Donner et al. (2011)
10	Hadley Centre Global Environmental Model, version 2 – Carbon Cycle (HadGEM2-CC)	Met Office Hadley Centre, United Kingdom	1.25° × 1.875°	Jones et al. (2011)
11	L'Institut Pierre-Simon Laplace Coupled Model, version 5A, medium resolution (IPSL-CM5A-MR)	Institut Pierre Simon Laplace, France	1.25° × 2.5°	Dufresne et al. (2013)
12	L'Institut Pierre-Simon Laplace Coupled Model, version 5B, low resolution (IPSL-CM5B-LR)		1.9° × 3.75°	
13	Model for Interdisciplinary Research on Climate, version 5 (MIROC5)	Atmosphere and Ocean Research Institute (The University of Tokyo), National Institute for Environmental Studies, and Japan Agency for Marine-Earth Science and Technology, Japan	1.4° × 1.4°	Watanabe et al. (2010)
14	Model for Interdisciplinary Research on Climate, Earth System Model (MIROC-ESM)	Japan Agency for Marine-Earth Science and Technology	2.8° × 2.8°	Watanabe et al. (2011)
15	Model for Interdisciplinary Research on Climate, Earth System Model, Chemistry Coupled (MIROC-ESM-CHEM)			
16	Max Planck Institute Earth System Model, low resolution (MPI-ESM-LR)	Max Planck Institute for Meteorology, Germany	1.9° × 1.9°	Giorgetta et al. (2013)
17	Max Planck Institute Earth System Model, mixed resolution (MPI-ESM-MR)			
18	Meteorological Research Institute Coupled Atmosphere-Ocean General Circulation Model, version 3 (MRI-CGCM3)	Meteorological Research Institute, Japan	1.12° × 1.125°	Yukimoto et al. (2012)
19	Meteorological Research Institute Earth System Model, version 1 (MRI-ESM1)		1.12° × 1.125°	Yukimoto et al. (2011)
20	Norwegian Earth System Model, version 1, intermediate resolution (NorESM1-M)	Norwegian Climate Center, Norway	1.9° × 2.5°	Bentsen et al. (2013)

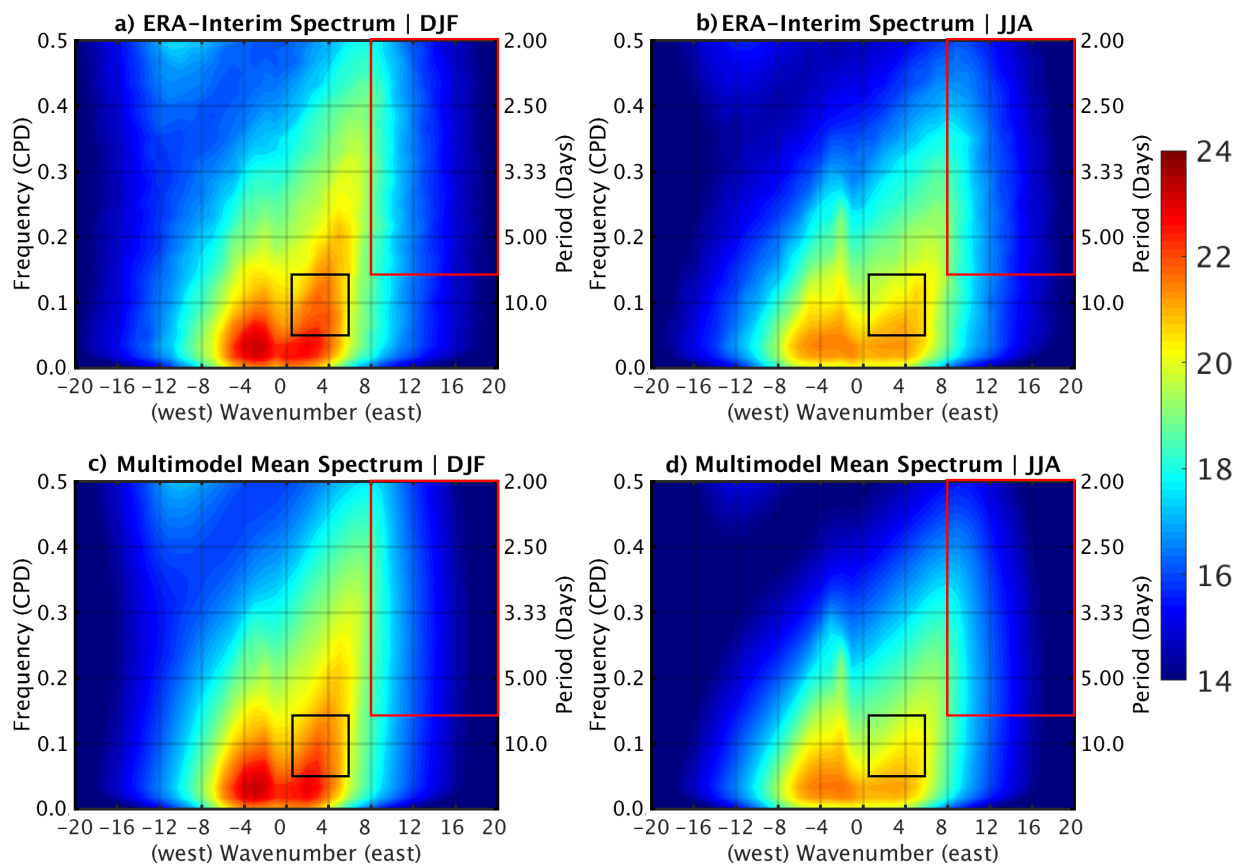


Figure 1: The 1979–2005 mean winter (left) and summer (right) wavenumber-frequency power spectrum of daily 500 hPa geopotential height (Z500) over the Northern midlatitudes (40°–60°N) for (a–b) ERA-Interim and (c–d) for the 20–CMIP5 model average. The black (red) box represents longwaves (shortwaves). The frequency units are in cycles per day (CPD).

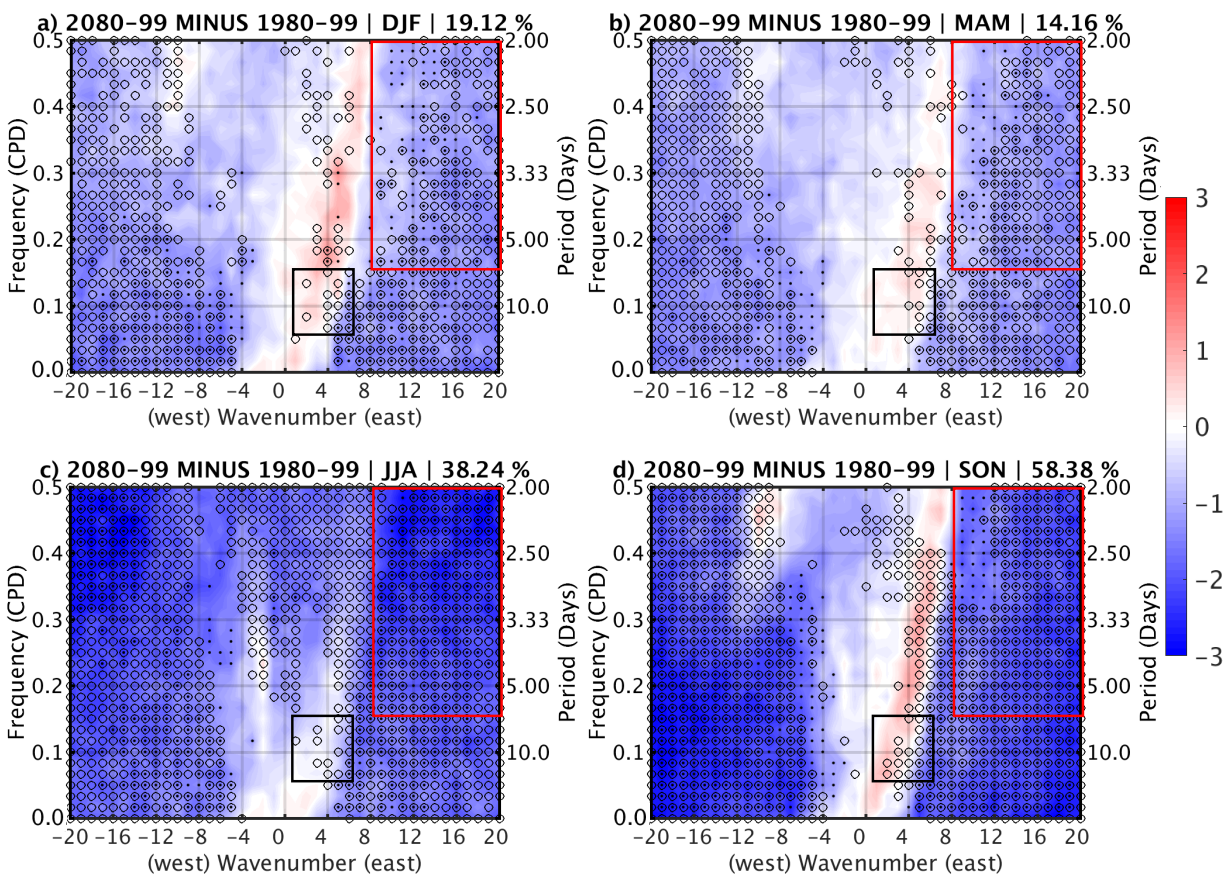


Figure 2: The 20 CMIP5 model-averaged relative percentage change in \log_e spectral power of daily Z500 for 2080–2099 minus 1980–1999 for each season. Stippling indicates where the change is statistically significant at the 5% level. Circles denote that 85% of the models agree on the sign of the change. The percentage of grid points that exhibit both statistical significance and model agreement is shown in the title of each panel. The black (red) box represents longwaves (shortwaves).

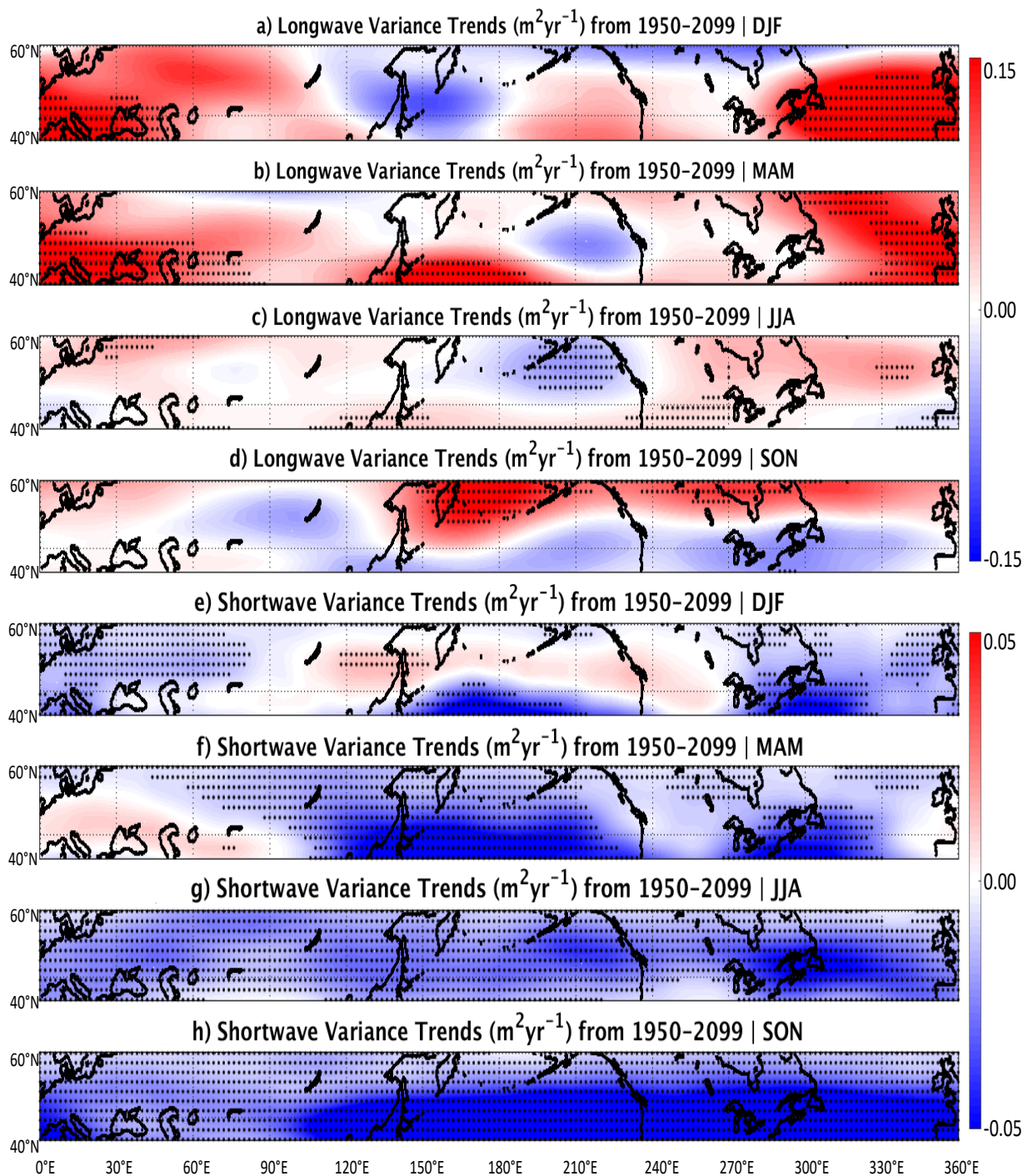


Figure 3: The 20 CMIP5 model-averaged trends in the variance of (a–d) longwaves and (e–h) shortwaves for each season over the Northern midlatitudes. Stippling represents significance at the 5% level.

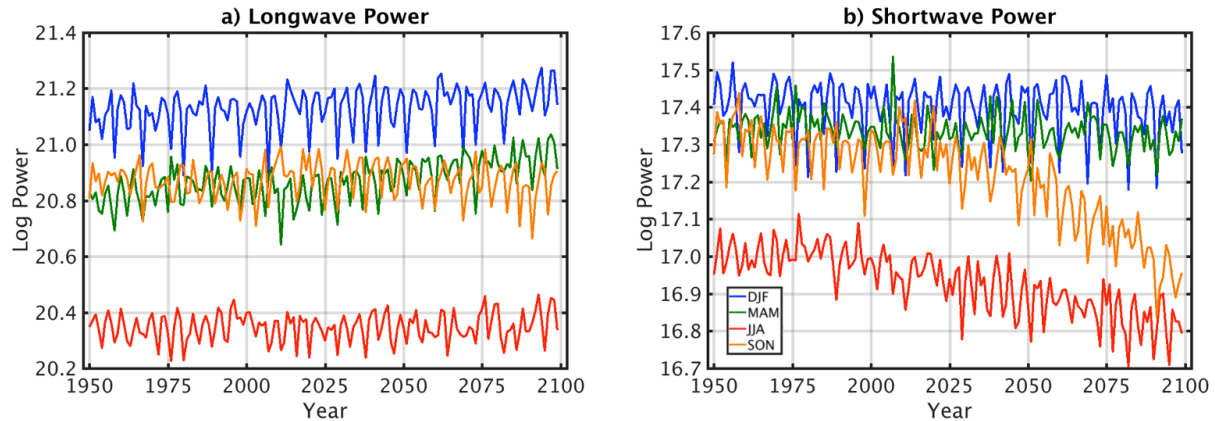


Figure 4: The 20 CMIP5 model-averaged time series of the mean \log_e spectral power of Z500 over $40^\circ\text{--}60^\circ\text{N}$ for a) longwaves and b) shortwaves from 1950–2099 for DJF, MAM, JJA, and SON. In a) and b), one unit of \log_e spectral power was added to the JJA time series for visualization purposes. The linear trends of the time series are all statistically significant at the 5% level except for JJA and SON in a).

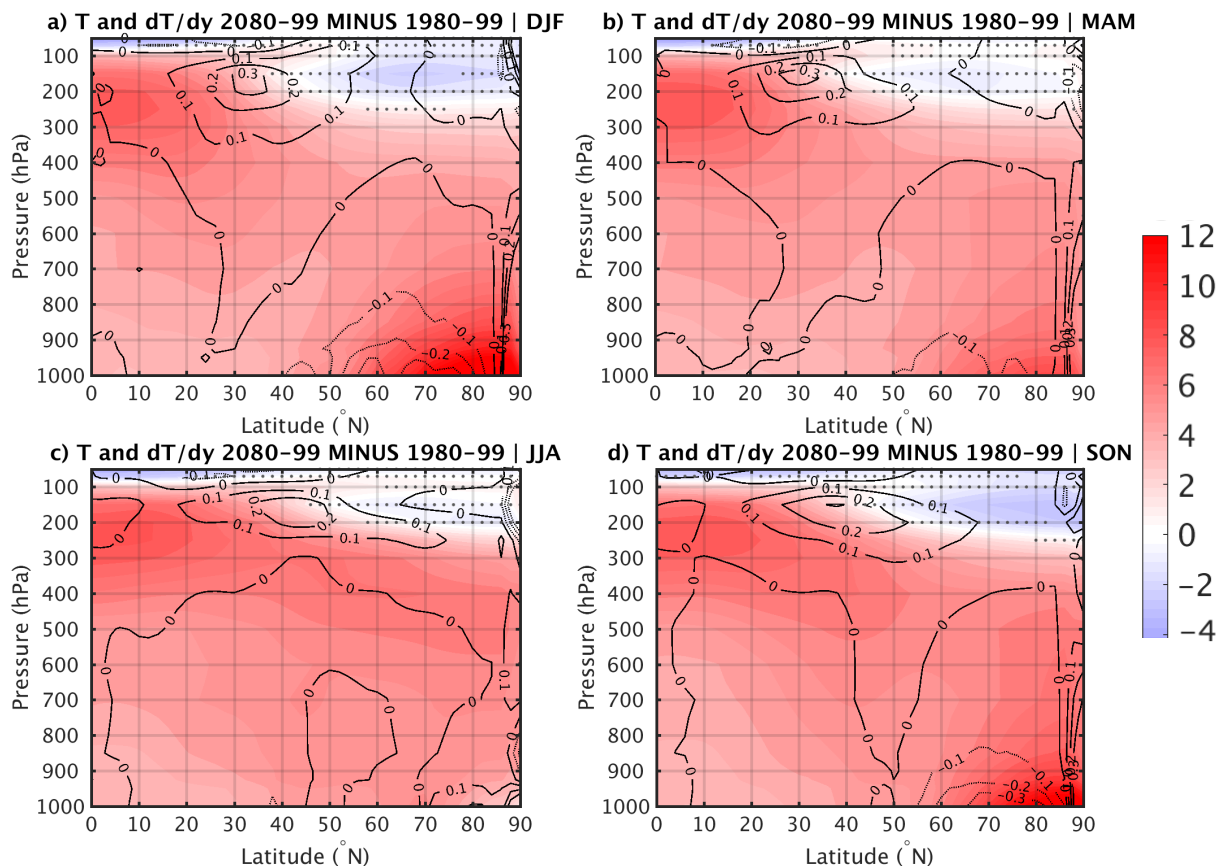


Figure 5: The 20 CMIP5 model-averaged zonal-mean air temperature change (T , K; color shading) and meridional temperature gradient change (dT/dy , K/lat ; contours) from the Arctic toward the Equator for the RCP8.5 scenario (i.e., 2080–2099) minus the historical period (i.e., 1980–1999). Areas where the change in air temperature is not significant at the 5% level are denoted by gray stippling.